

Segmental front line dynamics of randomly pinned ferroelastic domain walls

S. Puchberger^{1,*}, V. Soprunyuk¹, and W Schranz^{1†}

¹*University of Vienna, Faculty of Physics, Boltzmannngasse 5, A-1090 Wien, Austria*

M. A. Carpenter

*University of Cambridge, Department of Earth Sciences,
Downing Street CB2 3EQ, Cambridge, United Kingdom.*

(Dated: February 13, 2019)

Dynamic Mechanical Analysis (DMA) measurements as a function of temperature, frequency and dynamic force amplitude are used to perform a detailed study of the domain wall motion in LaAlO_3 . In previous DMA measurements Harrison, *et al.* [PRB **69**, 144101 (2004)] found evidence for dynamic phase transitions of ferroelastic domain walls in LaAlO_3 . In the present work we focus on the creep-to-relaxation region of domain wall motion using two complementary methods. We determine, additionally to dynamic susceptibility data, waiting time distributions of strain jerks during slowly increasing stress. These strain jerks, which result from self-similar avalanches close to the depinning threshold, follow a power-law behaviour with an energy exponent $\varepsilon = 1.7 \pm 0.1$. Also, the distribution of waiting times between events follows a power-law $N(t_w) \propto t_w^{-(n+1)}$ with an exponent $n = 0.9$, which transforms to a power-law of susceptibility $S(\omega) \propto \omega^{-n}$. The present dynamic susceptibility data can be well fitted with a power law, with the same exponent ($n=0.9$) up to a characteristic frequency $\omega \approx \omega^*$, where a crossover from stochastic DW motion to the pinned regime is well described using the scaling function of A.A. Fedorenko, *et al.* [PRB **70**, 224104 (2004)].

PACS numbers: 89.75.Da, 75.60.Ch, 45.70.Ht

I. INTRODUCTION

Understanding domain wall motion in ferroic materials is not only of pure scientific interest, but is also important for technical applications¹⁻⁴. Movements of domain walls (DW's) subject to external forces were shown to cause anomalously high values of susceptibility in some ferroelectrics⁵⁻⁸ and ferroelastics⁹⁻¹³ below the phase transition temperature T_c . The domain wall response is very sensitive to changes of external conditions, i.e. temperature, frequency, applied field, etc. In some systems, freezing of domain wall motion occurs at temperatures $T_f < T_c$ where the DW's can no longer follow the dynamically applied external force. As a result, the susceptibility drops down to the domain-averaged value. Such behaviour was found for example in dielectric measurements of KH_2PO_4 (KDP)¹⁴ and $(\text{NH}_2\text{CH}_2\text{COOH})_3 \cdot \text{H}_2\text{SO}_4$ (TGS)¹⁵ and in elastic measurements of KMnF_3 ^{9,16}, PbZrO_3 ¹³ and LaAlO_3 ¹¹.

As noticed, domain freezing dynamics shares some similarities to glass freezing dynamics⁷. For example it was found that the relaxation time for domain wall motion follows Vogel-Fulcher behaviour for KDP ($T_{VF} \approx 69 \text{ K}$), DKDP ($T_{VF} \approx 191 \text{ K}$) and TGS ($T_{VF} \approx 32 \text{ K}$). Vogel-Fulcher type domain freezing was also found in KMnF_3 doped with 0.003 % Ca ($T_{VF} \approx 55 \text{ K}$)¹⁰, whereas Arrhenius behaviour was detected for pure KMnF_3 ¹⁷. Meanwhile, Ren, *et al.*¹⁸⁻²⁰ found evidence for *strain glass* behaviour in ferroelastic martensites, i.e. $\text{Ti}_{50-x}\text{Ni}_{50+x}$, through a Vogel-Fulcher type relaxation time dependence, typical field-cooling/zero-field-cooling signatures²⁰ as well as the observation of

dynamic nanodomains which freeze out below T_g at a size of about 20-25 nm. In all these systems, impurities and/or defects seem to play a major role for the freezing process.

Very recently, Salje, *et al.*²¹ argued that domain boundary patterns can evolve glass-like states even without any defect induced disorder, which led them to the notion of *domain glass*. Indeed, large-scale molecular dynamics simulations^{22,23} of a ferroelastic crystal, with domain walls mimicked by a simple two dimensional spring model with a sheared (ferroelastic) ground state, show that DW movements under applied shear deformation follow Vogel-Fulcher behaviour at a certain temperature-regime. They found that pinning/depinning processes also appear as a consequence of domain jamming even if no extrinsic defects are present.

Regardless of whether or not defects are present in a sample, there is general consensus that domain wall pinning is a prerequisite for domain freezing. In the domain glass, the twin patterns involve a very high number of twin intersections which act as pinning centres. In other cases, domain walls are pinned at randomly distributed defects. In LaAlO_3 the determined values of activation energy suggest that domain walls are predominantly pinned by oxygen vacancies¹¹. The basic idea to explain a finite Vogel-Fulcher temperature⁷ $T_{VF} > 0$ is then that the pinning becomes correlative with decreasing temperature, leading to an increase of the effective pinning region²⁴ ΔR . This would imply that the collective pinning energy, U_{CP} , diverges at T_{VF} as $U_{CP} = U/(T - T_{VF})$. This is very appealing, since the concept of increasing (with decreasing T) cooperative

length scales^{25,26}, which leads to a diverging relaxation time at finite temperature, turned out to be very fruitful for glass forming liquids. It is only natural to check if a similar scenario applies also for the domain freezing problem.

The main purpose of the present work was to study the pinning-depinning process of ferroelastic domain walls (DW's) in detail as a function of temperature, frequency and applied external force. As an example we used the perovskite crystal LaAlO_3 , since many aspects of DW movement have been studied^{11,12,27-29} and can be used for comparison.

Domain wall pinning effects were already studied some time ago by measuring jerky responses of a system to slowly changing external conditions. For example in ferromagnetic DW's³⁰⁻³² it is known as *Barkhausen noise*. There were serious doubts if a similar crackling noise behaviour could be detected in a crystal with ferroelastic domains, since, due to elastic compatibility, ferroelastic domain walls are rather flat, implying a huge Larkin length and no pinning-depinning transition. However, Salje and Harrison^{27,28} found that jerky avalanches also occur during ferroelastic DW propagation. For LaAlO_3 , the pinning-depinning process was shown²⁸ to be mainly effective at the front line of the needle tips (Fig.1) which, opposed to the planar parts of the ferroelastic DW's, can easily break into smaller (nanoscale) segments of various length. Recently Gao *et al.*³³ studied the switching dynamics of individual ferroelastic domains in thin $\text{Pb}(\text{Zr}_{0.2}\text{Ti}_{0.8})\text{O}_3$ films by using in situ TEM. They found ferroelastic switching mainly to occur at the highly active needle tips in ferroelastic domains. These needle tips are shown to be broken into segments of various length of one to few nm's.

Harrison *et al.*²⁷ measured the movement of a single needle domain in LaAlO_3 under weak external stress at the critical depinning threshold and found discrete jumps of the needle tip of varying amplitude due to the pinning/depinning of wall-segments to defects. Tracking the movement of the needle tip $x(t)$ yields the dissipated energy via the kinetic energy $E \sim v^2 = (dx/dt)^2$. They found that the distribution of energies follows a power law $N(v^2) \propto (v^2)^{-\epsilon}$ behavior with an energy exponent of $\epsilon = 1.8 \pm 0.2$. A similar phenomenon of the jerky movement of *many* DW's in LaAlO_3 and PbZrO_3 was found recently³⁴ to have a power law distribution of the maximum drop velocities squared $N(v_m^2) \propto (v_m^2)^{-1.6 \pm 0.2}$.

In the present work we determine additionally the distribution $N(t_w)$ of waiting times between successive jerks, which are related to the energy landscape of the DW segments in the presence of defects (most probably oxygen vacancies in the case of LaAlO_3), and compare the calculated complex susceptibilities with frequency dependent elastic susceptibility data. We show that the DW response of LaAlO_3 at low frequency of the external stress shows up in three regimes of the complex elastic susceptibility, separated by dynamic phase transitions: sliding at $\omega\tau_{DW} < 1$, stochastic or creep regime (at

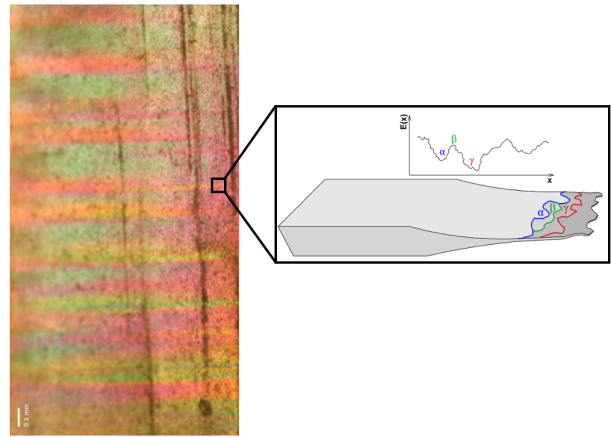


FIG. 1. Polarizing microscopy image of a LaAlO_3 sample and a schematic of a tip of a wedge-shaped needle domain with the propagating front line at the right. The front line is wavy and adapts to the various defect fields.

$\omega \gtrsim \omega^*$) and the pinned regime at $\omega > \omega^*$.

Section II presents details about the samples and the experimental measurement technique. In section III we show temperature dependent elastic susceptibility data at various frequencies, as well as the results of static and dynamic stress scans. We also show waiting time distributions determined from strain jerks at slowly increasing stress and compare the (Laplace transformed) results with dynamic susceptibility data obtained from frequency scans at different temperatures.

II. EXPERIMENTAL

For our present study, single crystals of lanthanum aluminate were used. LaAlO_3 is a perovskite crystal and exhibits a phase transition to an improper ferroelastic phase. At the phase transition temperature, $T_c = 823\text{K}$, the crystal structure changes from cubic $\text{Pm}\bar{3}\text{m}$ to rhombohedral $\text{R}\bar{3}\text{c}$ ²⁹. A typical domain structure of a LaAlO_3 sample at room temperature in its rhombohedral phase is shown in Fig.1.

Experiments were carried out using the technique of Dynamic Mechanical Analysis (DMA). The measurements were performed under two different operating modes of the DMA: static stress scans and dynamic stress scans of varying frequency, temperature and dynamic force. Static stress scans were performed to measure the sample height $h(t)$ as a function of time and external stress. The external force was slowly increased with time at rates of 3-15mN/min.

By way of contrast, dynamic stress scans involve a sinusoidally varying force, F_D . Apart from the dynamic force, a static force, F_S (which is approximately 15% larger than the dynamic force), is applied as well, ensuring that the sample remains in contact with the support edges (see Fig. 2). The DMA measures the amplitude u

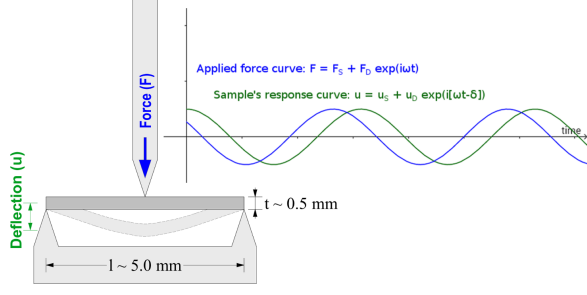


FIG. 2. Dynamic force and response signals using the DMA technique with dynamic stress mode and three-point-bending geometry of the DMA.

and phase lag δ of the mechanical response via electromagnetic inductive coupling and calculates certain components of the real and imaginary parts of the complex elastic compliance, S^* , depending on the orientation of the sample with respect to the applied force. In three-point-bend geometry, the distance between the sample's support edges l is usually much larger than the sample width, $l \gg w$, leading to the complex elastic compliance (in direction \vec{p} perpendicular to the applied force) of the form¹¹:

$$S^*(\vec{p}) = \frac{4t^3 w F_D}{l^3 u} e^{-i\delta} \quad (1)$$

where t is the sample thickness. The complex elastic compliance S_{ij} is related to the elastic constant tensor C_{ij} as $S_{ij} = C_{ij}^{-1}$ and to the real and imaginary parts of the complex Young's modulus $Y^* = Y' + iY''$ as

$$S' = [Y'(1 + \tan^2 \delta)]^{-1} \quad \text{and} \quad S'' = Y'' |Y^*|^{-2} \quad (2)$$

Static stress scans were conducted using the Pyris Diamond DMA (Perkin Elmer) because this device is able to apply a force up to 10 N, in contrast to the DMA7e which only allows a maximal force of 2.5 N. The resolution of the force is 0.002 N and the resolution of the sample height is about 3 nm. Although the relative accuracy of DMA measurements is about 1%, the absolute accuracy is usually not better than 20%. For this reason, all plots are shown here in relative units, i.e. normalized at an appropriate temperature. For dynamic stress scans, the DMA7e (Perkin Elmer) was used because, in contrast to the Diamond DMA, it is possible to set initial values for the dynamic and static forces simultaneously. With the Diamond DMA it is only possible to set an intentional strain. The device regulates static and dynamic stresses according to the sample's stiffness until the required strain is reached.

Regarding the sample geometry, three-point-bending was used for all measurements. The LaAlO_3 samples were cut in small rods of approximate size $5 \times 1.8 \times 0.5$

mm³, and were placed on two supports with distance 4.2 mm. The force is applied from above halfway along the sample length using an electromechanical force motor. The maximum temperature used was 620 K, for technical reasons.

III. RESULTS

A. Dynamic stress scans - Dynamic susceptibility

This section presents the results of dynamic stress measurements in LaAlO_3 where both the frequency and dynamic force amplitude were varied. It should be noted that Harrison *et al.*^{11,12} have already performed detailed DMA-measurements on LaAlO_3 . However, since we intend to compare our strain drop data, i.e. $\epsilon(\sigma(t), T)$, with the DMA data of $Y'(\sigma, f, T)$ and $Y''(\sigma, f, T)$, we performed DMA measurements in order to have a complete set of data from the same sample for comparison.

Temperature scans below T_c from room temperature to 623 K with varying measuring frequency are depicted in Fig.3. During these experiments the dynamic and static stresses were fixed at values of $F_D = 300$ mN and $F_S = 336$ mN. The frequency was changed after each temperature scan. As previously found²⁹, the low frequency response of the sample at temperatures above ≈ 470 K is dominated by domain wall motion in the domain sliding mode ($\omega\tau_{DW} < 1$) which induces superelastic softening. At lower temperatures, the DW's gradually freeze out as reflected in an increase of modulus Y' and a peak in Y'' at $\omega\tau_{DW} = 1$. The motion of DW's shows a strong frequency dependence. They can respond to the externally applied stress as long as the characteristic relaxation time τ_{DW} for DW movement is small enough in comparison with the measurement frequency. With decreasing temperature, τ_{DW} increases and the DW's can no longer follow the applied stress. If $\omega\tau_{DW} > 1$, this freezing of DW motion is accompanied by a re-hardening of the sample and the elastic response turns to the domain averaged value. The Y'' -peak shifts to higher temperatures with increasing frequency. For a Cole-Cole relaxation process, the domain wall relaxation time can be extracted from the Y'' diagram via determining the shift of the peak maximum, which appears at $\omega\tau_{DW} = 1$.

A Cole-Cole relaxation is used for fitting $Y'' = S'' |Y^*|^2$ in the crossover region, where $\omega\tau_{DW}(T) < 1 \rightarrow \omega\tau_{DW}(T) > 1$, with

$$S^*(\omega) = S_\infty + \frac{\Delta S^{DW}}{1 + (i\omega\tau_{DW})^\mu}. \quad (3)$$

Here S_∞ denotes the elastic compliance in the high frequency limit, where $\omega\tau_{DW} \gg 1$, and ΔS^{DW} refers to the DW-induced softening. The exponent μ leads to a broadening (if $\mu < 1$) of the Debye relaxation, which is obtained in the limit $\mu = 1$. In agreement with the results of Ref.29 a Cole-Cole function fits the data quite

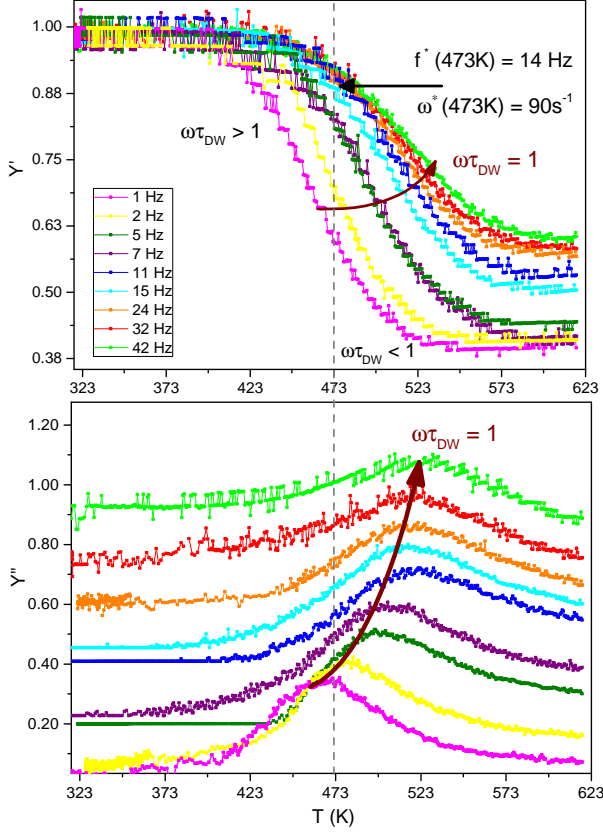


FIG. 3. Temperature dependencies of the real part of Young's modulus Y' in relative units (top) and the imaginary part Y'' (bottom) for LaAlO_3 measured at $F_D = 300$ mN, $F_S = 336$ mN and at different frequencies. Y'' curves are shifted for clarity.

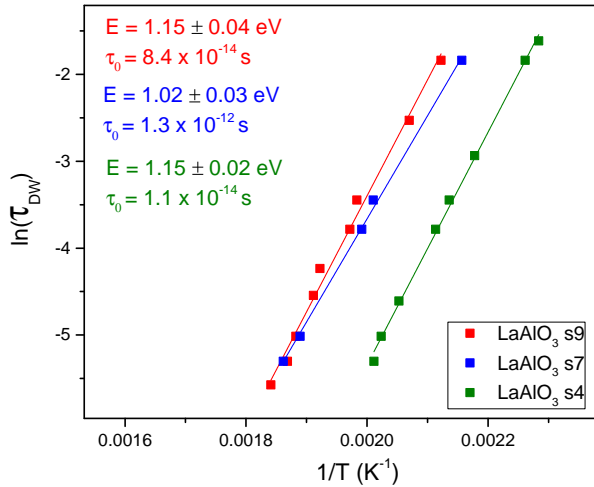


FIG. 4. Temperature dependence of the relaxation time of domain wall motion plotted in semi-logarithmic scale. The LaAlO_3 curves correspond to different samples labeled s4, s7, s9. Samples s9 and s7 were cut from the same piece of LaAlO_3 , whereas sample s4 was cut from a different piece. The solid lines correspond to Arrhenius-fits. Data points of sample s9 are derived from the curves of Fig.3.

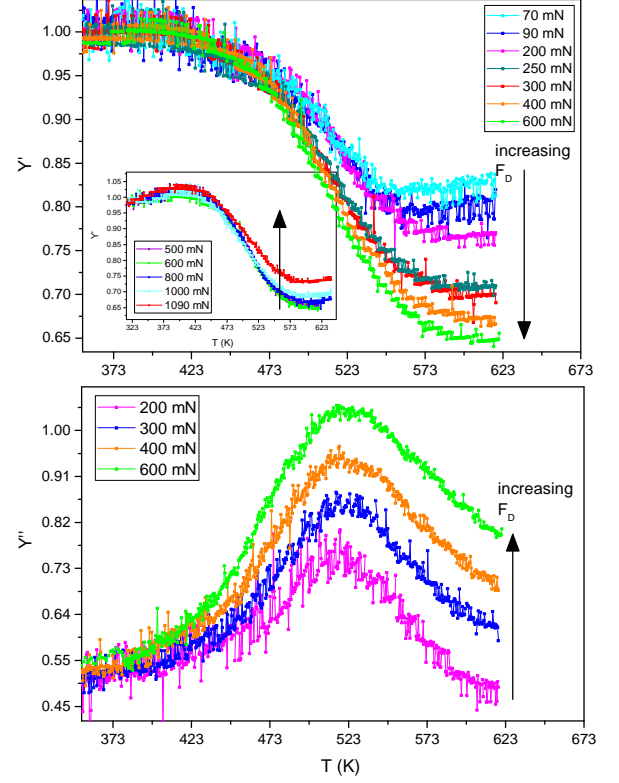


FIG. 5. Temperature dependencies of Y' of normalized Young's modulus (top) and Y'' (bottom) of LaAlO_3 measured at 24 Hz and at different dynamical forces ($F_S = 1.2 \cdot F_D$). Y'' curves are shifted for clarity. Inset shows further measurements at increasing forces leading to a re-hardening.

well, if one allows for the broadening parameter μ to vary between ca. 0.5 and 0.7 as a function of temperature. The relaxation time for LaAlO_3 is then well fitted (Fig.4) with an Arrhenius law

$$\tau_{DW} = \tau_0 \exp(E/k_B T), \quad (4)$$

yielding an activation energy, $E = 1.15 \pm 0.04$ eV ≈ 110 kJ/mol, for the LaAlO_3 sample (s9) used for measurements depicted in Fig.3. For another sample (s7), a slightly lower value, $E = 1.02 \pm 0.03$ eV ≈ 96 kJ/mol, was determined. Both values are quite similar to the results of Harrison et al.²⁹ ($E = 0.985, 0.881$ and 0.891 eV).

Further investigations of the DW behavior involve variation of the applied external dynamic force. Fig.5 shows results for real Y' and imaginary Y'' parts of Young's modulus at different amplitudes of the dynamic force, F_D , at a constant frequency of 24 Hz. Increasing the dynamic force amplitude leads to an increasing softening of the sample up to a value of approximately $F_D = 600$ mN. Further increase of the dynamic force amplitude above 600 mN results in a re-hardening (see inset of Fig.5). Such a behavior is also reflected in an increase of the Y'' peak with increasing dynamic force, followed by a decrease at values above 600 mN. A similar pattern is found

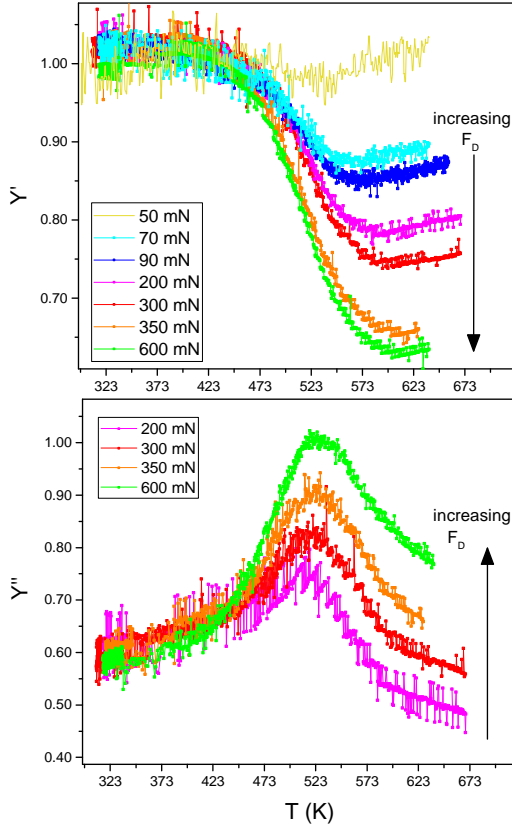


FIG. 6. Temperature dependencies of Y' of normalized Young's modulus (top) and Y'' (bottom) of LaAlO_3 measured at 32 Hz and at different dynamical forces ($F_S = 1.2 \cdot F_D$). Y'' curves are shifted for clarity.

for other frequencies (see e.g. Fig.6). The re-hardening at forces >600 mN is due to saturation effects, which occur when needle tips retract to the side of the sample where they no longer contribute to the macroscopic strain²⁹.

From the curves in Fig.5 and 6, data points for Fig.7 were extracted to show the real part of Young's modulus as function of dynamic force amplitude for 1 Hz, 24 Hz and 32 Hz at a temperature of 523 K. These plots show that the Young's modulus decreases rather abruptly at a certain stress value associated with the critical depinning force F_ω which is necessary to set the DW's in motion. Below F_ω the DW's remain pinned. The critical depinning force increases with increasing frequency from about 100 mN at 1 Hz to 200 mN at 24 Hz and 300 mN at 32 Hz. At forces $F_D > F_\omega$, the DW's are able to escape their pinning sites and the superelastic regime is entered. Upon increasing the dynamic force further, Y' decreases and remains at a low value until the dynamic force amplitude exceeds the upper threshold stress, F_t , of about 700 mN at 1 Hz and 800 mN at 24 Hz. At stresses above the upper threshold stress, $F_D > F_t$, the saturation regime is reached and the modulus increases again. Hence, the threshold stress separates the superelastic from the satu-

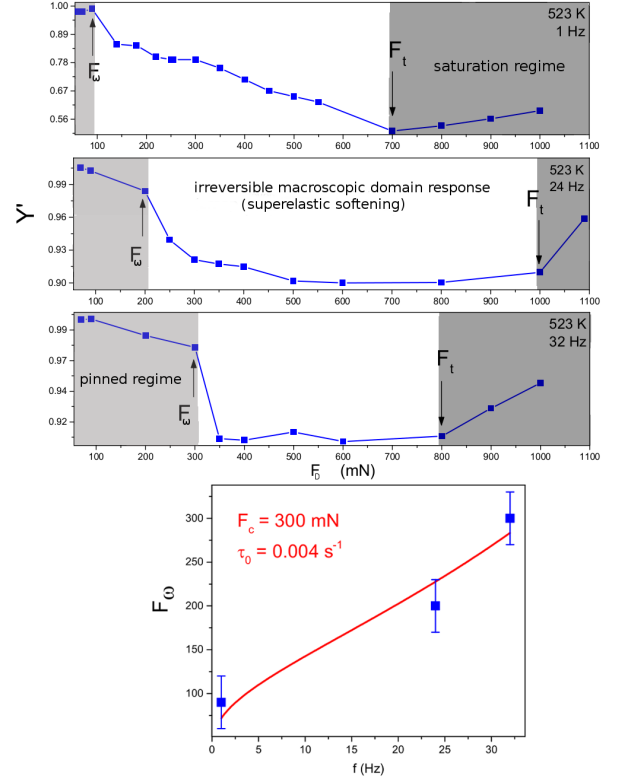


FIG. 7. Dynamic force dependence of the real part of Young's modulus at 1Hz (top), 24 Hz (middle), 32Hz (bottom) at a temperature of 523 K. The decrease in modulus above a critical value of dynamical force is associated with the unpinning of domain walls, displaying a dynamic phase transition at F_ω . The lowest plot shows the critical depinning force F_ω as a function of frequency.

ration regime. Harrison et al.¹¹ showed that the critical depinning stress, F_ω , is a function of temperature because thermal fluctuations enable DW's to unpin. The results of the present study demonstrate that F_ω is a function of frequency as well.

In addition, frequency scans at constant temperatures, shown in Fig.8, were performed to further investigate the changes in Young's modulus which occur close to the domain freezing temperature. The static and dynamic forces were fixed at $F_S = 448$ mN and $F_D = 400$ mN, and measurements were performed within a temperature range 303 K - 573 K, i.e. starting in the domain freezing regime up to the superelastic regime. At lower temperatures, 303 K - 373 K, the modulus shows hardly any variation with frequency. With increasing temperature, the overall value of the modulus decreases and shows a strong variation of frequency. The dispersion is maximal at temperatures of about 470 K. Increasing the temperature further, the dispersion disappears again.

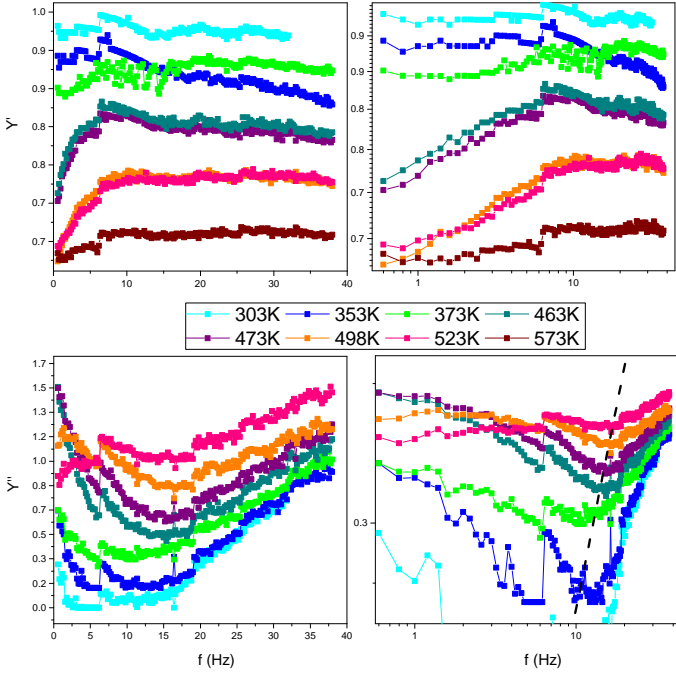


FIG. 8. Real part Y' of Young's modulus (top) and imaginary part Y'' (bottom) as functions of frequency on linear (left) and log-log (right) scale. $F_S = 448$ mN, $F_D = 400$ mN.

B. Static stress scans - Strain intermittency

To study the pinning-depinning process of DW segments in more detail, we have performed static stress scans at various temperatures. Fig.9 shows the height evolution of LaAlO_3 with slowly increasing static stress at different temperatures. At low temperatures (blue curves), the sample height follows a stretched-exponential relaxation envelope punctuated by jerks of varying amplitude. The jerks are manifestations of pinning-depinning events of DW's to defects or due to mutual jamming of DW's.

Fig. 10 shows the corresponding squared drop velocity peaks derived from the height evolution $h(t)$ with time as $v_m^2 = (dh/dt)_m^2$. They vary over several orders of magnitude and result from about 4000 (at 323 K) single discontinuous strain bursts with about 200 positive velocity jumps, i.e. backward movements of the domain walls. These back-jumps were neglected for further calculations because including them yielded the same statistical results.

For calculation of the power law exponents, the peak data were logarithmically binned (bin size = 0.1) and plotted in a histogram. Fig.11 shows the log-log plot of the distributions of squared drop velocity maxima calculated from the statistical characteristics of height drops $\Delta h(t)$. $N(v_m^2)$ is calculated from the squared temporal derivative $v(t)^2 = (dh/dt)^2$ of the sample height $h(t)$. The curves at lower temperatures (curves in different blue shades), i.e. in the frozen regime ($\omega\tau_{DW} > 1$) are fitted

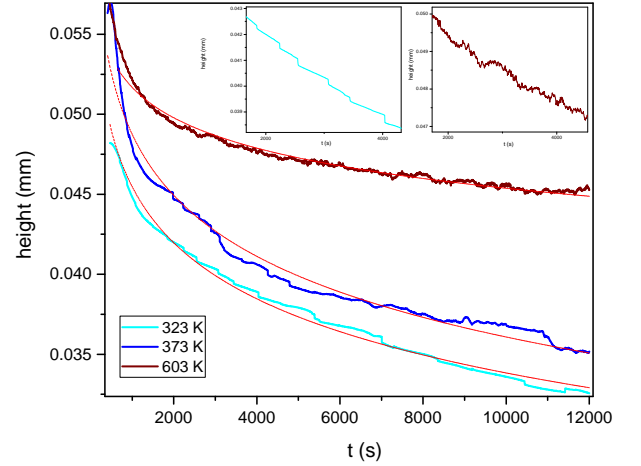


FIG. 9. Height evolution during a compression experiment of LaAlO_3 at different temperatures. The applied force is increased at the rate 10 mN/min from 10 to 2000 mN. (Curves are shifted for clarity.) The red curves correspond to stretched-exponential fits ($\propto e^{-(t/\tau)^\beta}$ with $\beta \approx 0.003$). Insets show magnifications of $h(t)$ revealing different evolutions of height at 323 K (left) and 603 K (right).

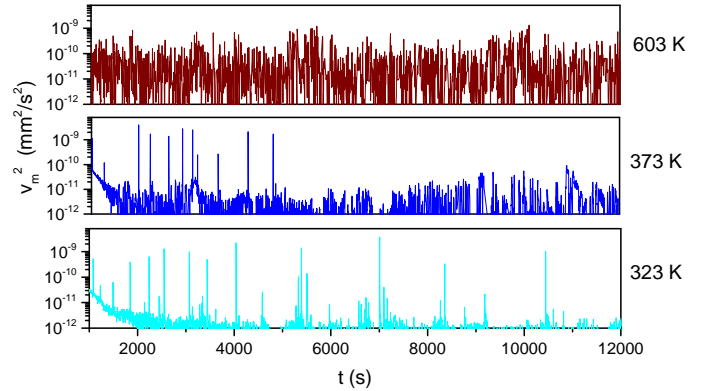


FIG. 10. Squared drop velocity peaks $v_m^2 = (dh/dt)_m^2$ derived from the height measurements (Fig. 9) of LaAlO_3 .

by a power-law $N(v_m^2) \propto (v_m^2)^{-\epsilon}$ with $\epsilon = 1.7 \pm 0.1$. This exponent value agrees very well with the exponent value of Harrison *et al.*²⁷, $\epsilon = 1.8 \pm 0.2$, who studied the jerky propagation of *one* needle.

At higher temperatures (curves in red shades) the response of the sample differs considerably. An increase in the number of energy jerks (Fig.10) with increasing temperature is observed, together with an exponential distribution of $N(v_m^2)$. This crossover is in agreement with recent computer simulations of a ferroelastic switching process at different temperatures^{22,23}, and is most probably due to thermal fluctuations which at high temperature ease the motion of domain wall segments²⁴ of various length l_i with a rate of $\tau(l_i)^{-1} = \tau_0^{-1} e^{-E(l_i)/T}$. The distribution of waiting times t_w between successive events is shown in Fig.12. It also yields

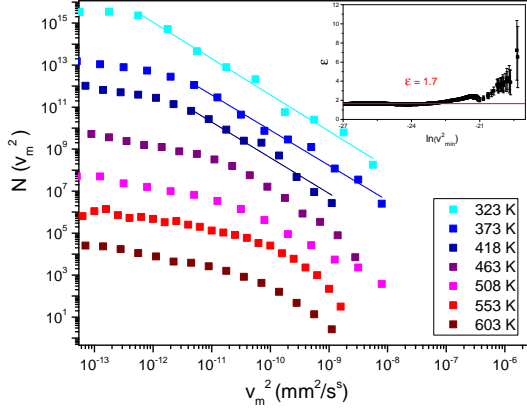


FIG. 11. Log-log plot of the distribution $N(v_m^2)$ of maximum drop velocities squared of LaAlO_3 at different temperatures. Curves are calculated from the similar color curves of Fig.9. (Curves are shifted for clarity.) The linear fits correspond to power laws with exponent of $\epsilon = 1.7 \pm 0.1$. The inset shows a corresponding maximum likelihood plot.

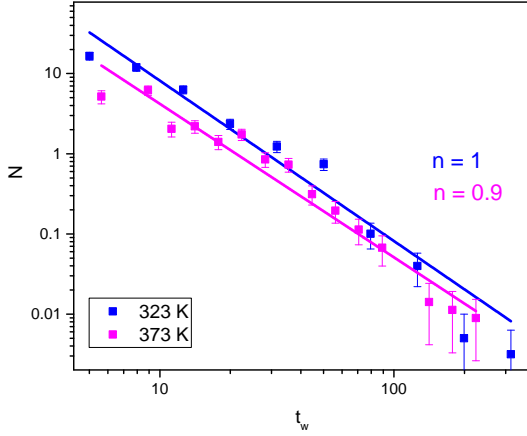


FIG. 12. Waiting time distributions $N(t_w)$ corresponding to measurements shown in Fig.9 for LaAlO_3 , calculated from the time intervals between successive v_m^2 peaks of Fig.10.

a power-law $N(t_w) \propto t_w^{-(n+1)}$, with $n \approx 0.9$.

IV. DISCUSSION

Fig.3 shows real and imaginary parts of Young's modulus of LaAlO_3 as a function of temperature at different frequencies. The behaviour is very similar to the DMA-data of Harrison, *et al.*²⁹. At sufficiently high temperature (say above ≈ 550 K, depending on f) the domain walls can perform macroscopic displacements in response to the applied dynamic force, $F_D > F_w$, leading to a DW induced superelastic softening at $\omega\tau_{DW} \ll 1$. In this superelastic regime it was shown⁴⁷ that the DW motion induced elastic compliance ΔS^{DW} of Eq.(3) can be written as

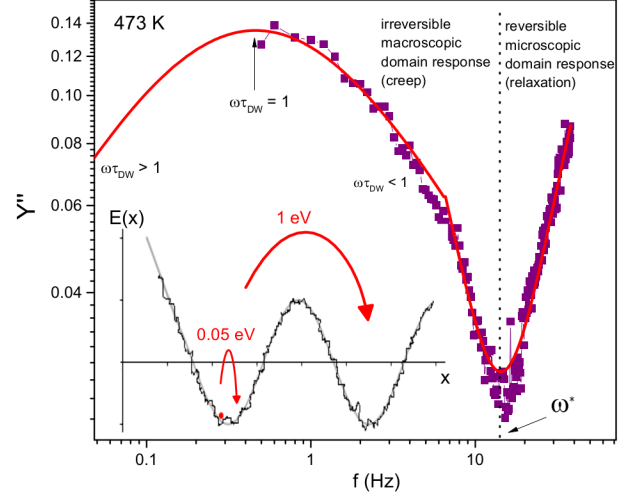


FIG. 13. Frequency dependence of Y'' of LaAlO_3 at $T=473$ K, showing two dispersion regions. The part far enough below $\omega^*/2\pi \approx 15$ Hz is well fitted with a Cole-Cole relaxation function. In the region around $f \approx \omega^*/2\pi$, a scaling function⁵¹, Eq.(10), describes the data quite well.

$$\Delta S^{DW}(T) \propto \frac{N_w}{B} \eta^2(T) \quad (5)$$

where N_w is the number of domain walls, η the order parameter and B is the 4th order coefficient of the Landau-expansion. Eq. (5) describes the domain wall induced superelastic softening⁴⁸ in the region $\omega\tau_{DW} \ll 1$ for many ferroelastic systems.

In the derivation of Eq. (5) the needle shape of ferroelastic walls plays an essential role. Contrary to ferroelectrics and ferromagnetics, a system of parallel striped ferroelastic domain walls is unstable, because of the lack of a field that corresponds to the depolarization or demagnetization field. However, at the tips of ferroelastic needles, long range elastic fields are created, which act in a very similar way to the stray fields in ferroelectrics or ferromagnetics, and stabilize⁴⁹ an array of ferroelastic needles. The dynamics of such a domain wall array in LaAlO_3 have been described phenomenologically²⁹ in the range $\omega\tau_{DW} < 1$ by a Cole-Cole function, Eq. (3). Combining Eqs. (3) and (5) we obtain

$$\Delta S^{DW} = S^\infty + \text{const.} \frac{N_w}{B} \eta^2(T) \frac{1}{1 + (i\omega\tau_{DW})^\mu} \quad (6)$$

The behaviour of Fig.3 can be well described with Eq. (6) and μ varying with temperature between ca. 0.5 - 0.7. Moreover, a fit of the data (e.g. Fig.3) yields an Arrhenius dependence of the DW relaxation time τ_{DW} (Fig.4) with an activation energy $E \approx 1$ eV, which is close to the activation energy commonly associated with oxygen vacancy diffusion in oxide ceramics⁵⁰. With decreasing temperature, τ_{DW} increases and a decreasing

fraction of DWs can follow the applied dynamic force. The rest of the needles are pinned. This increase of the ratio of static to mobile needle tips with decreasing temperature was observed²⁹ by in situ optical microscopy during DMA measurements.

Inspecting Fig.8, we realize that in the vicinity of the domain freezing regime (around 470 K at 1 Hz), there are at least two dispersion regions. A regime below $f^* \approx 15$ Hz and another one above f^* . With the temperature dependence of the domain wall relaxation time τ_{DW} (Fig.4), one finds that the region much below f^* corresponds to the region of macroscopic DW motion. For example at 470 K, $\tau_{DW} \approx 0.06$ s and, accordingly, the region of macroscopic domain wall motion, i.e. where $\omega\tau_{DW} < 1$ to $\omega\tau_{DW} = 1$, is below approximately 3 Hz. Indeed, in the region below ca. 8 Hz, $Y''(f)$ can be well fitted (Fig.13) with the Cole-Cole relaxation Eq. (3) and the parameters obtained from the fits of the T-dependent measurements (Fig.3).

In the region above $\omega\tau_{DW} = 1$, the macroscopic domain wall motion gradually freezes out and only segments of DWs can move in the random potential. For $f < f^*$ it is assumed that, on the time scale given by $2\pi/\omega$ (f = measurement frequency), the center of mass of the field-driven DW segments probes different local minima of the energy landscape, corresponding to different metastable DW configurations (see inset of Fig.13). This region has been referred to as the stochastic regime⁵¹. We can resort to a large amount of theoretical work³⁵⁻⁴⁰ to understand the behaviour of DW motion in this region. For example it was shown^{35,51} that the distribution $\psi(t_w)$ of waiting times $t_w(L) = \tau_0 \exp[E_B(L)/T]$ for hops of DW segments of length L between metastable states separated by energy barriers $E_B(L) \simeq U_c(L/L_c)^\theta$ (U_c is the typical barrier on the Larkin scale L_c and $\theta = 2\zeta + D - 2$, D ...dimension of the interface = 2 for DWs, ζ ...roughness exponent of DWs = 2/3 for Random Bond impurities⁵⁴. This yields $\theta = 4/3$.) scales as a power law at large times, i.e.

$$\psi(t_w) \propto (t_w/\tau_0)^{-(n+1)}. \quad (7)$$

Here

$$n = (T/U_c)(\nu - 1), \quad (8)$$

and $\nu > 2$ determines the size distribution $n(L) \propto L^{-\nu}$ of DW segments. The dynamic response in this regime ($f < f^*$), which often is called the creep regime, is then given as

$$S(\omega) = S^\infty [1 + (i\omega\tau_0)^{-n}]. \quad (9)$$

For frequencies corresponding to $\omega \gg \omega^*$ the DW segments are captured in the valleys, i.e. only relaxational reversible motion of internal modes occurs. In the region

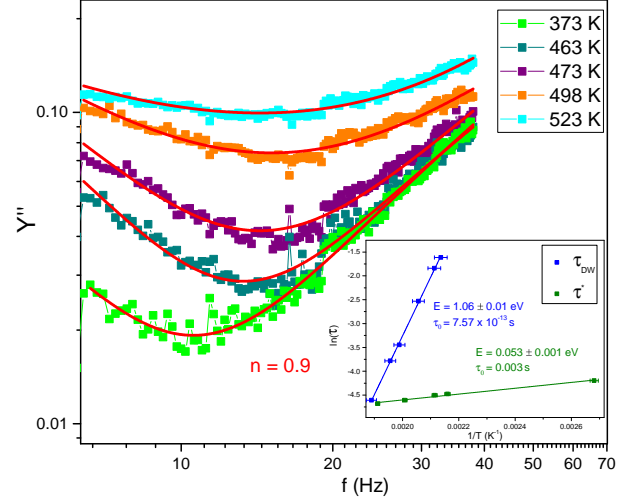


FIG. 14. Frequency dependence of Y'' at various temperatures in the domain freezing regime (data points). The red lines are the best fits using Eq.(10) with $n=0.9$ and $\kappa=1.2 \pm 0.2$. $F_S = 448$ mN, $F_D=400$ mN

$\omega \gtrsim \omega^*$, the imaginary part of the dynamic susceptibility was represented by a scaling function⁵¹

$$S''(\omega) = a\omega^{-n} \left[1 + \frac{1}{2\kappa - 1} \left(\frac{\omega}{\omega^*} \right)^\kappa \right]^{2n} \quad (10)$$

Fig.14 shows the measured frequency dependencies of Y'' at different temperatures in the domain freezing region. The data can be perfectly fitted using Eq.(10) with $n=0.9$ and $\kappa = 1.2 \pm 0.2$.

At this stage it should be stressed that there is perfect agreement between the exponents ($n \approx 0.9$) which are determined by two quite independent experimental methods. The first is from frequency dependent measurements of the dynamic susceptibility $S^*(\omega)$ at a given temperature (Fig's. 8 and 14), and the second is from the intermittent DW response to a slowly increasing stress (Fig's. 9 and 10), yielding the distribution of waiting times (Fig.12) between successive jerks. Moreover, using Eq.(8) with $n=0.9$, we obtain with $\nu - 1 \approx 1$, $T/U_c \approx 0.9$. This implies that, at $T \approx 400$ K, i.e. the temperature, where the crackling noise exponent was measured, the elementary pinning energy is of the order of $U_c \approx 0.04$ eV. Interestingly enough, this value of U_c is rather similar to the value determined from the frequency scans (Fig.14). Indeed, we found an Arrhenius dependence of the depinning frequency $\omega^* = \tau_0^{-1} \exp(-\Delta E/T)$ (see inset of Fig.14), with an activation energy $\Delta E \approx 0.05$ eV that is close to the value of $U_c \approx 0.04$ eV.

Along the same line of reasoning, we can also understand the frequency dependence of the threshold force F_ω (Fig.7), which was shown³⁷ to obey the relation

$$F_\omega = F_c \left[\frac{U_c}{T \ln(\frac{1}{\omega\tau_0})} \left(1 - \frac{F_\omega}{F_c} \right)^\theta \right]^{1/\mu}. \quad (11)$$

With $\theta = 4/3$ for random bond impurities, and $\mu = \theta/(2 - \zeta) = 1$ for $\zeta = 2/3$, we can approximate Eq.11 as

$$F_\omega = \frac{F_c}{1 + \frac{T \cdot \ln(1/(\omega\tau_0))}{U_c}}, \quad (12)$$

which describes the observed (Fig.7) increase of F_ω with increasing ω rather well. Eq. 11 also explains the $\sim 1/T$ dependence of the depinning force found by Harrison, *et al.* (Fig.10 of Ref.11).

The observed similarity between $\Delta E \approx U_c$ can be well explained with the threshold frequency⁵¹

$$\omega^* = \tau_0^{-1} \exp \left[-\frac{U_c}{T} \cdot \left(\frac{F_c}{F} \right)^\mu \right] = \tau_0^{-1} \exp \left(\frac{\Delta E}{T} \right) \quad (13)$$

and the value $F_c \approx 300$ mN, obtained from the fit (Fig.7). During frequency scans (Fig.14) the applied force was $F \approx 400$ mN. The values of $F_c \approx 300$ mN and $F \approx 400$ mN support the assumption $\Delta E = \frac{U_c}{T} \left(\frac{F_c}{F} \right)^\mu \approx \frac{U_c}{T}$.

V. CONCLUSIONS

Up to this time, work on "elastic" interfaces in random environments of ferroics has been mainly focused on ferromagnetic and ferroelectric systems. In the present study we investigated the ac-response of elastic DWs in LaAlO₃. Similarly to many other systems, where a competition between disorder (due to defects) and order (due to interfacial elasticity) leads to a rugged energy landscape with many metastable states, this is also the case for ferroelastic DWs in the presence of defects.

By measuring the complex linear susceptibility of LaAlO₃ at low frequency we found clear effects of such a complex energy landscape. The data can be well modeled within a scaling approach by taking account of local pinning and motion of DW segments under random pinning forces^{36,51}. At temperatures $T \approx T_f$ around the domain freezing regime, where the macroscopic motion of DWs has already stopped during one period of the alternating force ($\omega\tau_0 > 1$), segments of DWs of length L can still overcome local barriers of height $E_B(L)$, even at forces $F_\omega < F_c$, where F_c is the pinning force at $T=0$ K. This leads to an irreversible creep like wall motion with $S''(\omega) \propto \omega^{-n}$ with $n \approx 0.9$. To study this non-Debye response also in the time domain, we measured the distribution of waiting times $\psi(t_w)$ needed to overcome the energy barriers, which, according to theory (e.g. Ref.³⁵), should scale as $\psi(t_w) \propto t_w^{-(n+1)}$. Although these measurements of $\psi(t_w)$ are rather complementary (based on strain bursts during slow compression) to the frequency dependent susceptibility measurements, there is a remarkable agreement between both methods, both lead to $n=0.9$.

In summary, the present results suggest that DW dynamics in disordered ferroic materials are rather universal. Moreover, ferroelastic domain walls are ideal objects to study the dynamics of elastic manifolds driven through a random medium. Dynamic mechanical analysis is a very appropriate method for its study, since it can be used in a complementary way to provide both the dynamic elastic response in the frequency domain (dynamic susceptibility) and in the time domain (through strain intermittency measurements).

Further measurements on various systems have to be done to understand the DW dynamics around $\omega\tau_{DW} \approx 1$ in more detail, so as to reveal the microscopic origin of domain freezing and to see if the observed deviations of τ_{DW} from Arrhenius behaviour, found in some systems, are manifestations of a domain glass.

Acknowledgments The present work was supported by the Austrian Science Fund (FWF) Grant No. P28672-N36.

* sabine.puchberger@univie.ac.at

† wilfried.schranz@univie.ac.at

¹ J.R. Whyte and J.M. Gregg, Nature Commun. **6**, 7361 (2015).

² L.J. McGilly, P. Yudin, L. Feigl, A.K. Tagantsev and N. Setter, Nature Nanotech. **10**, 145 (2015).

³ G. Catalan, J. Seidl, R. Ramesh and J. Scott, Rev. Mod. Phys. **84**, 119 (2012).

⁴ J.R. Whyte, R.C.P. McQuaid, P. Sharma, C. Canalias, J.F. Scott, A. Gruvermah and J.M. Gregg, Adv. Mater. **26**, 293 (2014).

⁵ V. Mueller, Y. Shchur, H. Beige, S. Mattauich, J. Glinne-mann, and G. Heger, Phys. Rev. B **65**, 134102 (2002).

⁶ V. Mueller, Y. Shchur, H. Beige, A. Fuith, and S.

Stepanow, Europhys. Lett. **57**, 107 (2002).

⁷ Y.N. Huang, X. Li, Y. Ding, Y.N. Wang, H.M. Shen, Z.F. Zhang, C.S. Fang, S.H. Zhuo and P.C.W. Fung, Phys. Rev. B **55**, 16159 (1997).

⁸ Y. Park, Solid State Commun. **113**, 379 (2000).

⁹ W. Schranz, A. Tröster, A.V.Kityk, P. Sondergeld and E.K.H. Salje, Europhys. Letters **62**, 512 (2003).

¹⁰ W. Schranz, P. Sondergeld, A. V. Kityk, and E. K. H. Salje, Phys. Rev. B **80**, 094110 (2009).

¹¹ R.J. Harrison and S.A.T. Redfern, Phys. Earth Planet. Interiors **134**, 253 (2002).

¹² R.J. Harrison, S.A.T. Redfern and J. Street, Am. Min. **88**, 574 (2003).

¹³ S. Puchberger, V. Soprunyuk, A. Majchrowski, K. Roleder

- and W. Schranz, Phys. Rev. B **94**, 214101 (2016).
- ¹⁴ J. Bornarel and B. Torche, Ferroelectrics **132**, 273 - 283 (1992).
 - ¹⁵ Y. Huang, X. Li, Y. Ding, H. Shen, Z.F. Zhang, Y.N. Wang, C.S. Fang and S.H. Zhu, Journal de Physique IV Colloque, **6** (C8), 815 - 818 (1996).
 - ¹⁶ A.V. Kityk, W. Schranz, P.Sondergeld, D. Havlik, E.K.H. Salje and J.F. Scott, Phys. Rev. B **61**, 946 (2000).
 - ¹⁷ E.K.H. Salje and H. Zhang, J. Phys.: Condens. Matter **21**, 035901 (2009).
 - ¹⁸ S. Sarkar, X. Ren and K. Otsuka, Phys. Rev. Lett. **95**, 205702 (2005).
 - ¹⁹ X. Ren, Phys. Status Solidi B **251**, 1982 (2014).
 - ²⁰ X.Ren, Y.Wang, Y.Zhou, Z.Zang, D.Wang, G.Fan, K.Otsuka, T.Suzuki, Y.Ji, J.Zhang, Y.Tian, S.Hou, X.Ding, Phil. Mag. **90**, 141 (2010).
 - ²¹ E.K.H. Salje, X. Ding and O. Atkas, Phys. Stat. Sol. B **251**, 2061 (2014).
 - ²² E.K.H. Salje, X. Ding, Z. Zhao, T. Lookman and A. Saxena, Phys. Rev. B. **83**, 104109 (2011).
 - ²³ X. Ding, T. Lookman, Z. Zhao, A. Saxena, J. Sun and E.K.H. Salje, Phys. Rev. B **87**, 094109 (2013).
 - ²⁴ T. Nattermann and S. Brazovskii, Adv. Phys. **53**, 177 (2004).
 - ²⁵ G. Adam and J.H. Gibbs, J. Chem. Phys. **43**, 139 (1965).
 - ²⁶ S. Karmakar, C. Dasgupta and S. Sastry, PNAS **106**, 3675 (2009).
 - ²⁷ R.J. Harrison and E.K.H. Salje, Appl. Phys. Lett. **97**, 021907 (2010).
 - ²⁸ R.J. Harrison and E.K.H. Salje, Appl. Phys. Lett. **99**, 151915 (2011).
 - ²⁹ R.J. Harrison, S.A.T. Redfern and E.K.H. Salje, Phys. Rev. B **69**, 144101 (2004).
 - ³⁰ G. Durin and S. Zapperi, "The Science of Hysteresis", vol.II, G. Bertotti and I. Mayergoyz eds, 181-267 (Elsevier, Amsterdam, 2006).
 - ³¹ F. Colaiori, Adv. in Physics **57**, 287 (2008).
 - ³² G. Durin, F. Bohn, M.A. Corrêa, R.L. Sommer, P. Le Doussal and K. J. Wiese, Phys. Rev. Lett. **117**, 087201 (2016).
 - ³³ P. Gao, J. Briston, C.T. Nelson, et al., Nature Commun. **5**, 3801 (2014)
 - ³⁴ S. Puchberger, V. Soprunyuk, W. Schranz, A. Tróster, K. Roleder, A. Majchrowski, M.A. Carpenter and E.K.H. Salje, APL Materials **5**, 046102 (2017).
 - ³⁵ V.M. Vinokur, Physica D **107**, 411 (1997).
 - ³⁶ T. Nattermann, Y. Shapir and I. Vilfan, Phys. Rev. B **42**, 8577 (1990).
 - ³⁷ T. Nattermann, V. Pokrovsky and V.M. Vinokur, Phys. Rev. Lett.**87**, 197005 (2001).
 - ³⁸ M.V. Feigel'man and V.M. Vinokur, J. Phys. (France) **49**, 1731 (1988).
 - ³⁹ V.M. Vinokur, M.C. Marchetti and L.-W. Chen, Phys. Rev. Lett. **77**, 1845 (1996).
 - ⁴⁰ A.B. Kolton, A. Rosso, T. Giamarchi and W. Krauth, Phys. Rev. B **79**, 184207 (2009).
 - ⁴¹ J. Baró , Á. Corral, X. Illa, A. Planes, E.K.H. Salje, W. Schranz, D.E. Soto-Parra and E. Vives, Phys. Rev. Lett. **110**, 088702 (2013).
 - ⁴² S. Lemerle, J. Ferré, C. Chappert, V. Mathet, T. Giamarchi and P. Le Doussal, Phys. Rev. Lett. **80**, 849 (1998).
 - ⁴³ W. Kleemann, J. Dec and R. Pankrath, Ferroelectrics **291**, 75 (2003).
 - ⁴⁴ W. Kleemann, J. Dec and R. Pankrath, Ferroelectrics **286**, 21 (2003).
 - ⁴⁵ W. Kleemann, T. Braun, J. Dec and O. Petravic, Phase Transitions **78**, 811 (2005).
 - ⁴⁶ W. Kleemann, Annu. Rev. Matt. Res. **37**, 415 (2007).
 - ⁴⁷ W. Schranz, Phys. Rev. B **83**, 094120 (2011).
 - ⁴⁸ W. Schranz, H. Kabelka, A. Sarras and M. Burock, Appl. Phys. Lett. **101**, 141913 (2012).
 - ⁴⁹ J. Torr  s, C. Roucau, and R. Ayroles, Phys. Status Solidi (a) **70**, 193 (1982).
 - ⁵⁰ X.P. Wang and Q.F. Fang, Phys. Rev. B **65**, 064304 (2002).
 - ⁵¹ A.A. Fedorenko, V. Mueller and S. Stepanow, Phys. Rev. B **70**, 224104 (2004).
 - ⁵² J. Guyonnet, E. Agoritsas, S. Bustingorry, T. Giamarchi, and P. Paruch, Phys. Rev. Lett. **109**, 147601 (2012).
 - ⁵³ G. Catalan, H. B  a, S. Fusil, M. Bibes, P. Paruch, A. Barth  l  my, and J.F. Scott, Phys. Rev. Lett. **100**, 027602 (2008).
 - ⁵⁴ Indeed values for ζ close to $2/3$ have been found for some ferroelectric domain walls pinned by random bond disorder, see e.g. Ref.52 and 53.